

THE DEUTERIUM ABUNDANCE TOWARD Q1937–1009

SCOTT BURLES^{1,2} AND DAVID TYTLER^{1,3}

Department of Physics, and Center for Astrophysics and Space Sciences University of California, San Diego C0424, La Jolla, CA 92093-0424

Received 1997 August 18; accepted 1998 January 9

ABSTRACT

We present a new measurement of the deuterium-to-hydrogen ratio (D/H) in the Lyman limit absorption system at $z = 3.572$ toward Q1937–1009. Tytler, Fan & Burles (TFB) made the first extragalactic detection of deuterium in this absorption system, which remains the best location for a high-accuracy measurement of primordial D/H. Their detailed analysis of Keck spectra gave a low value of $D/H = 2.3 \pm 0.3 \pm 0.3 \times 10^{-5}$ (1σ statistical and systematic errors). Now we present a new method to measure D/H in QSO absorption systems. We avoid many of the assumptions adopted by TFB; we allow extra parameters to treat the continuum uncertainties, include a variety of new absorption models that allow for undetected velocity structure, and use the improved measurement of the total hydrogen column density by Burles & Tytler. We find that all models, including contamination, give an upper limit of $D/H < 3.9 \times 10^{-5}$ (95% confidence). Both this and previous analyses find contamination to be unlikely in this absorption system: a χ^2 analysis in models without contamination gives $D/H = 3.3 \pm 0.3 \times 10^{-5}$ (67% confidence), which is higher but consistent with the earlier results of TFB, and a second measurement of D/H toward Q1009+2956. With calculations of standard big bang nucleosynthesis (SBBN) and the assumption that this measurement of D/H is representative of the primordial value, we find a high baryon-to-photon ratio, $\eta = 5.3 \pm 0.4 \times 10^{-10}$. This is consistent with primordial abundance determinations of ${}^4\text{He}$ in H II regions and ${}^7\text{Li}$ in the atmospheres of warm metal-poor Population II stars. We find a high value for the present-day baryon density, $\Omega_b h^2 = 0.0193 \pm 0.0014$, which is consistent with other inventories of baryonic matter, from low to high redshift: clusters of galaxies, the Lyman alpha forest & the cosmic microwave background.

Subject headings: galaxies: abundances — quasars: absorption lines

1. INTRODUCTION

Standard big bang nucleosynthesis (SBBN; Wagoner, Fowler, & Hoyle 1967; Walker et al. 1991; Smith, Kawano, & Malaney 1993; Krauss & Kernan 1995; Copi, Schramm, & Turner 1995) predicts that a measurement of the primordial ratio D/H will give the most sensitive constraint on the cosmological baryon-to-photon ratio, η . Using the photon density measured from the temperature of the cosmic microwave background (CMB), we can then obtain the most sensitive constraint on $\Omega_b h^2$, the cosmological baryon density in units of the critical density, where $H_0 = 100 h \text{ km s}^{-1} \text{ Mpc}^{-1}$. Both η and Ω_b are fundamental cosmological parameters, and measurements of D/H in QSO absorption systems can determine both to 10% accuracy. When we compare measurements of the primordial abundances of different light elements, H, D and ${}^4\text{He}$ in particular, we test the SBBN theory predictions. Measurements of D/H in different astrophysical sites also constrains the history of star formation in these sites once the primordial value of D/H is established because D is totally destroyed (astrated) as gas is cycled through and ejected from stars (Epstein, Lattimer, & Schramm 1976).

Adams (1976) first suggested that deuterium could be measured in intergalactic gas clouds through Lyman absorption lines in the spectra of distant QSOs. Deuterium Lyman absorption lines are 82 km s^{-1} on the short wavelength side of the corresponding hydrogen Lyman lines, but Adams notes that D can be detected in only very select

absorption systems with simple velocity structures and high neutral hydrogen column densities, $N(\text{H I}) > 10^{17} \text{ cm}^{-2}$ (Lyman limit systems). For high redshifts, $z > 2.5$, the Lyman series is redshifted into the optical, and the lines are accessible to large ground-based telescopes. The Lyman absorption lines of D and H, and the Lyman continuum absorption of H I, constrain the column densities of D I and H I and provide a measurement of D I/H I. The timescale for H and D ionization equilibrium is very short (10^5 yr) in the photoionized intergalactic medium ($n_{\text{H}} \approx 10^{-3}$), and we assume that the ratio D I/H I is identical to D/H throughout this paper (Ikeuchi & Ostriker 1986).

The Lyman limit system at $z = 3.572$ toward Q1937–1009 is an ideal site to infer a primordial value for D/H. The system is very metal poor, less than 1/100 solar. Deuterium is destroyed as gas is cycled through stars, but metals are produced in the cycle and the system's low metallicity limits the amount of deuterium that could have been destroyed. The gas in the system also has very low internal velocities, which can limit the amount of kinetic energy input through any high-energy phenomena, such as supernovae or gamma ray sources.

In Tytler, Fan, & Burles (1996; hereafter TFB), we presented high-resolution spectra of Q1937–1009 and made the first measurement of D/H in a QSO absorption system. This system has a high total neutral hydrogen column density, $\log N(\text{H I}) = 17.86 \pm 0.02 \text{ cm}^{-2}$ (Burles & Tytler 1997), and the corresponding absorption is optically thick throughout the entire Lyman series. The deuterium feature is well determined by its profile in $\text{Ly}\alpha$, and the column density of D is well constrained.

In this paper, we advance the methods of TFB to place more robust constraints on D/H in this absorption systems. In § 2, we describe our new method of constraining D/H,

¹ Visiting Astronomer, W. M. Keck Telescope, California Association for Research in Astronomy.

² Present address: University of Chicago, 5640 South Ellis Avenue, Chicago, IL 60637.

³ Visiting Associate, European Southern Observatory.

and in § 3 we discuss the new results. In § 4, we calculate the abundances for a number of metals and discuss the ionization state of the system. In § 5, we compare our D/H value to the abundance of D in other sites, and to other light elements, and we show that our D/H is probably primordial.

2. CONSTRAINING D/H

We model the absorption spectrum along the QSO line of sight as a finite number of discrete absorbing components. Each component is modeled as a Voigt profile (Spitzer 1978) given by three parameters: column density (N), redshift (z), and velocity dispersion (b). At every wavelength, we sum the optical depth contribution of all absorption-line profiles in the model. The optical depth is converted to a normalized flux and convolved with the instrumental response. The model spectrum can then be directly compared to the observed spectrum. We use the observed spectrum described in TFB.

2.1. Previous Analysis

The TFB analysis was sophisticated since it was the first to simultaneously fit many metal and H lines and to separate thermal and turbulent contributions to line widths. However, it also used many assumptions that we now remove.

In TFB, we modeled the absorption system with two D/H components, labeled “blue” and “red.” The strong Ly α feature also required a third H I component (which contained only 1% of the hydrogen column) to obtain an adequate fit to the spectrum of the Lyman series. The positions of the two main components were “tied” to the velocity positions determined from the narrow metal lines that were asymmetric and well described by these two components. We fit the model to narrow regions of the spectrum containing only the Lyman lines of interest and did not include absorption from other Ly α lines along the line of sight. D/H was assumed to be equal in both components. The velocity dispersion of the red D line was determined from the dispersions of the corresponding H and metal lines in the red component. We found the value of D/H that gave the best fit to the data and the formal 1σ errors from the D and H column densities, $\log(D/H) = -4.64 \pm 0.06$. We investigated systematic errors due to incorrect continuum placement in the regions of Ly α and the Lyman limit and estimated the systematic error $\Delta \log(D/H) = 0.06$.

The TFB analysis found a consistent model and a well-defined value for the most likely value of D/H, but its limitations lay in the assumptions and in the calculation of confidence levels and the total errors on D/H.

2.2. Present Analysis

In this paper, we present major improvements in our analytic techniques. We measure D/H with a variety of models and free parameters. We add new free parameters to describe the unabsorbed quasar spectrum, which we use to normalize the absorption spectrum. Previously, we treated continuum uncertainties as systematic errors. The number and velocities of the D/H components are now also free parameters. We no longer require that the D and H lines have the same velocities as the metal lines. The D and H line profiles are constrained only by the spectra covering the Lyman series lines. To include all the uncertainties from the modeling into the final uncertainty of D/H, we perform a χ^2

analysis as a function of D/H. Formerly, we calculated the errors from a quadrature sum of the total column density uncertainties of D and H. By calculating χ^2 as a function of D/H, we can include the uncertainties from all the free parameters in our models, including the velocity dispersions, velocity positions, continuum levels, and column densities. The χ^2 function gives the relative likelihood of all values of D/H versus the best-fit value. The final confidence region can be directly calculated from the χ^2 function and can be considered more “comprehensive” than the uncertainties that we reported before.

2.2.1. Total Hydrogen Column Density

The most critical addition to the present analysis is a measurement of the total hydrogen column density, $N(\text{H I})_{\text{total}}$. From our detailed study of the Lyman continuum optical depth (Burles & Tytler 1997), we measured $N(\text{H I})_{\text{total}} = 17.86 \pm 0.02$, and we use this constraint for all models. $N(\text{H I})_{\text{total}}$ is much better constrained from the Lyman continuum absorption than from the Lyman series line profiles, which give $N(\text{H I})_{\text{total}} = 17.94 \pm 0.06 \pm 0.06$ (TFB), where the first error is statistical and the second is systematic. The new $N(\text{H I})_{\text{total}}$ provides a very strong constraint for the models, allows us to add more free parameters to the models to test a variety of models and minimize the model fit with respect to D/H.

2.2.2. New Models

Here we discuss the new models we have adopted to measure D/H. The absorbers in each model can be placed into one of two groups, depending on their association with the D/H absorption system (DHAS). The first group contains H I absorbers that will not show D I (also labeled “unassociated”), and the second group contains the high column H I absorbers that show D I and are associated with the DHAS. We refer to absorbers in the second group as the “main components.” For each unassociated absorber, we add three free parameters to the model, one each for N , b , and z . Each main component shows two lines, one of H I and the other D I. We also add one parameter for each line to allow a separation of b into T and b_{tur} , because in general $b(\text{H I})$ can differ from $b(\text{D I})$, but we tie three of the parameters in the two lines: $z(\text{H I}) = z(\text{D I})$, $T(\text{H I}) = T(\text{D I})$, and $b_{\text{tur}}(\text{H I}) = b_{\text{tur}}(\text{D I})$. In this paper, we do not use the metal lines to constrain D/H. The velocity dispersions of the main components are given by $b^2 = 163.84(T/m) + b_{\text{tur}}^2$, where T is temperature in units of 10^4 K, m is the atomic mass, and b is in units of km s^{-1} . For zero turbulent velocity dispersion, we recover the thermal relation for the H I and D I lines, $b(\text{H I}) = 2^{1/2}b(\text{D I})$. In all models, we require that $T > 5000$ K in the main components. Without this constraint, models that fit the data may include unobserved components with very low T . The background ionizing radiation is hard enough that the absorbing gas is unlikely to be cooler than a few times 10^4 K.

The results depend on assumptions we make when constructing the models. These assumptions include the number of D/H components, the total number of free parameters, and the spectral regions that we fit. The total number of free parameters is the sum of parameters of all the absorption components and the free parameters included in the continuum. For this analysis, we have chosen seven models, and we measure D/H for each. We can then compare the best-fit values of D/H for each model

TABLE 1
SPECTRAL REGIONS USED IN D/H MEASUREMENT

Region	λ_{\min}	λ_{\max}	Pixels	Order ^a
Ly α	5546.08	5568.57	301	5
Ly β	4687.50	4692.00	70	3
Ly γ	4445.60	4451.56	98	3
Ly δ	4340.40	4346.00	94	3
Ly ϵ	4284.70	4293.10	145	3
Ly6	4253.30	4257.06	63	3
Ly7	4232.15	4239.10	120	3
Ly9	4208.35	4213.10	82	3
Ly limit	4178.30	4196.56	325	3

^a Order of Legendre polynomial used for the continuum.

and assess the effects of the different assumptions used in each model. All seven models include the spectral regions listed in Table 1, the number of D/H components chosen for each model, and the 64 H I absorbers listed in Table 2.

The models are of three types. Models 1 and 2 are the simplest and include two and three D/H components, respectively, with no free parameters in the continuum. The continuum is held fixed at the initial placement of the unabsorbed continuum level, which is shown as the solid lines at unity in Figure 2. The other five models allow for free parameters in the continuum in each region. The number of allowed continuum free parameters in each region is shown in Table 2. The final two models have three D/H components but also allow for hydrogen contamination. In model 6, an extra hydrogen absorber is introduced at redshift $z = 3.570958$, which places H I Ly α at the position of D Ly α , and H I Ly β at D Ly β . In model 7, the extra hydrogen absorber is introduced at $z = 2.85670$, which places its Ly α at the position of D Ly β , in the blue wing of Ly β . The model parameters are summarized in Table 3.

2.2.3. Fitting Procedure

We use the Levenberg-Marquardt method to minimize χ^2 (Press et al. 1992). The details of the algorithm and computational techniques are presented in Burles (1998). The

algorithm iterates until it converges on the best-fit model. The χ^2 of the final fit is assumed to be the minimum χ^2 , χ_{\min}^2 .

A given model will have M free parameters, and the algorithm calculates an $M \times M$ covariance matrix for each iteration. The 1σ uncertainties can be directly calculated from the diagonal elements in the covariance matrix of the final iteration.

In all the models, we are specifically interested in one parameter, D/H. It is not straightforward to calculate the total uncertainty in D/H from the final covariance matrix directly, even if the errors are normally distributed. Because of the intrinsic blending of the H I and D I lines, the formal errors in column density are correlated. Instead, we choose to make D/H a free parameter in the models and calculate χ_{\min}^2 as a function of the parameter D/H.

We construct a list of D/H values and model the spectrum for each value in the list. By designating D/H in each model, we reduce the number of free parameters, M , by one for each D/H component in the model. Now each main component (components that have D absorption) has only four free parameters: $N(\text{H I})$, T , b_{tur} , and z . $N(\text{D I})$ is no longer free but is given by $N(\text{D I}) = N(\text{H I}) \times (\text{D/H})$. We assume that D/H is the same in all main components.

By constructing an array of χ_{\min}^2 as of function of D/H, we can calculate the most likely value of D/H and the confidence levels surrounding this value. We have effectively taken a cross section of the M -dimensional χ^2 function to calculate the uncertainties of the single parameter, D/H. The one-dimensional function, $\chi^2(\text{D/H})$, yields both the most likely value of D/H and confidence levels about the most likely value.

2.2.4. Continuum Level

Figure 1 shows the spectral regions stacked in velocity space. Figure 2 presents each spectral region separately on the vacuum heliocentric wavelength scale.

The unabsorbed QSO continuum is now allowed to vary to achieve the best fit. The QSO continuum is modeled by a low-order Legendre polynomial, which accounts for smooth variations in the continuum on scales of 100 km s^{-1}

TABLE 2
GROUP 1 LINES IN D/H MODELS

log N	b	z	log N	b	z	log N	b	z
12.73	30.3	3.58001	14.27	40.8	2.65975	14.34	33.1	2.48516
12.59	32.0	3.57881	14.76	31.8	2.65795	14.16	37.5	2.48387
12.88	18.2	3.57864	13.44	16.7	2.57458	12.64	19.8	2.48218
13.54	21.0	3.57846	14.59	35.4	2.57384	13.01	19.3	2.46537
13.39	17.1	3.57781	14.08	62.5	2.57216	12.51	11.0	2.46489
13.12	27.2	3.57749	13.84	26.4	2.57127	14.57	47.3	2.46359
13.62	20.7	3.57673	13.58	32.3	2.53110	12.70	18.4	2.46265
12.28	22.8	3.57584	13.43	24.0	2.53043	12.93	19.1	2.46216
13.24	63.4	3.57503	13.70	62.5	2.52962	13.84	70.2	2.45247
12.92	20.7	3.57381	12.31	9.3	2.52853	13.75	38.2	2.45109
15.40	31.1	3.57295	13.62	22.1	2.52785	14.17	34.1	2.44969
13.20	44.0	3.56964	13.39	43.7	2.52595	12.52	5.9	2.44885
12.39	22.7	3.56837	13.59	33.7	2.52506	14.00	28.7	2.44785
12.43	16.3	3.56760	14.04	28.6	2.50091	13.86	22.0	2.44761
13.63	34.5	3.56699	13.60	35.5	2.50053	13.13	9.3	2.44647
14.00	26.8	3.56640	12.80	10.7	2.49969	14.06	31.7	2.44450
14.31	32.9	3.56495	13.50	21.1	2.49948	13.53	20.9	2.44366
13.05	20.6	3.56427	13.18	30.9	2.49919	13.11	22.2	2.44332
13.42	33.3	3.56333	13.24	37.0	2.48705	14.00	26.4	2.44115
12.30	6.8	2.66147	13.18	21.4	2.48646	12.96	7.5	2.44042
12.96	20.5	2.66101	13.32	38.8	2.48615	13.60	28.5	2.43971
						13.83	8.9	2.43868

TABLE 3
D/H ABSORPTION MODELS

Model	Components ^a	D/H (-2σ) ^b	D/H (χ^2_{\min})	D/H ($+2 \sigma$) ^b	χ^2_{\min}	ν^c
1.....	2	-4.55	-4.51	-4.46	424.9	1097
2.....	3	-4.55	-4.48	-4.41	420.6	1093
3.....	2	-4.55	-4.51	-4.47	394.3	1069
4.....	3	-4.56	-4.49	-4.44	387.2	1065
5.....	4	-4.55	-4.48	-4.42	383.5	1061
6.....	3 ^d	-4.87	-4.59	-4.43	382.0	1062
7.....	3 ^e	-4.57	-4.49	-4.42	379.1	1062

- ^a Number of main components in fit.
^b 95% confidence levels from χ^2 test.
^c Degrees of freedom with 1298 pixels.
^d Additional contaminating hydrogen component at Ly α .
^e Additional contaminating hydrogen component at Ly β .

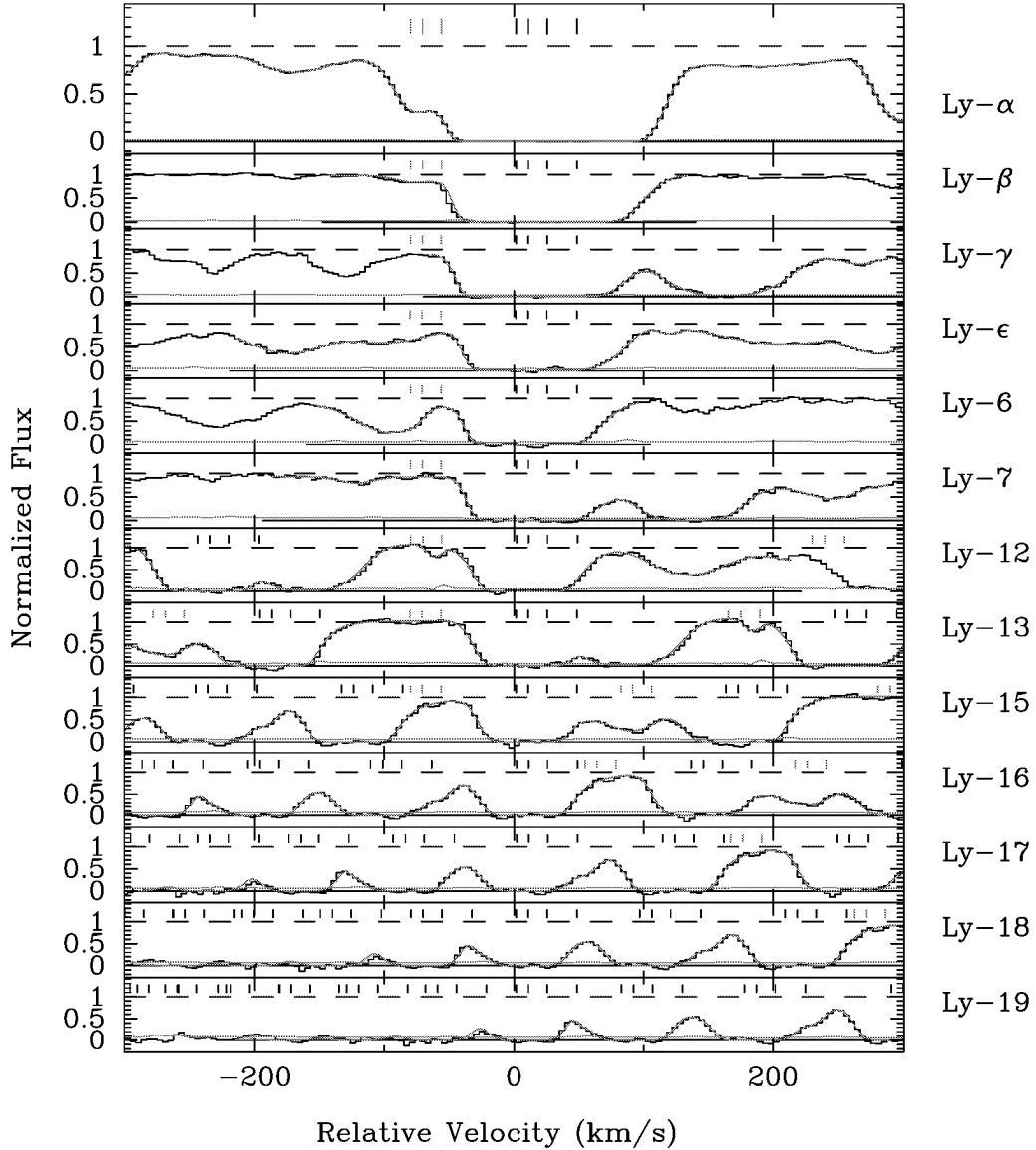


FIG. 1.—Velocity plots of the Keck High-Resolution Echelle Spectrograph (HIRES) spectrum containing Lyman series lines in the D/H absorption system toward Q1937–1009. Zero velocity corresponds to a redshift, $z = 3.572201$, which is identical to Fig. 1 in TFB. The Lyman limit region shows Ly12 through Ly19 in separate frames to emphasize the alignment of the entire Lyman series in velocity position. The data is the solid histogram; each bin corresponds to 1 pixel. The gray line tracing the data is the best-fit model with three components, model 4. The three light tick marks represent the positions of the deuterium Lyman lines, and the three solid ticks near $v = 0$ mark the corresponding hydrogen Lyman lines. The fourth solid tick marks an additional hydrogen absorber, which does not show deuterium. The solid horizontal line at zero flux shows the span of the region of interest around each Lyman line. For Ly α , the region of interest spans the entire velocity range shown in Fig. 1, while the other Lyman lines have smaller regions. We use all of the spectrum covering the Lyman series from Ly12 to the Lyman limit. Both the spectrum and model fit have been normalized to the unabsorbed quasar continuum, which was included in the fitting procedure. The 1σ error in the data values are shown by the dotted line near zero flux.

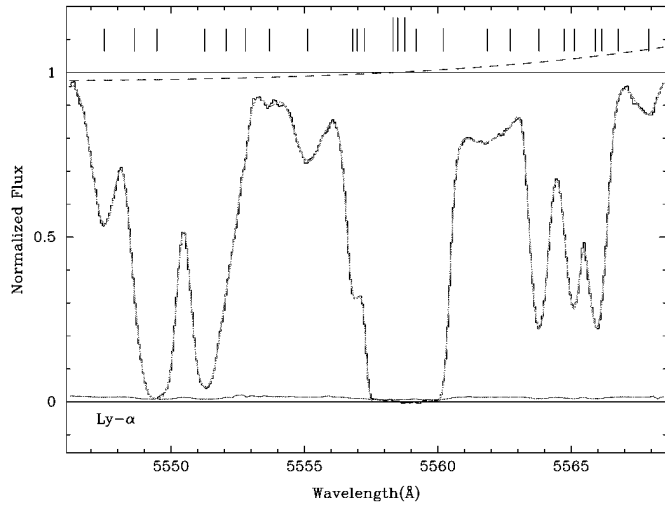


FIG. 2a

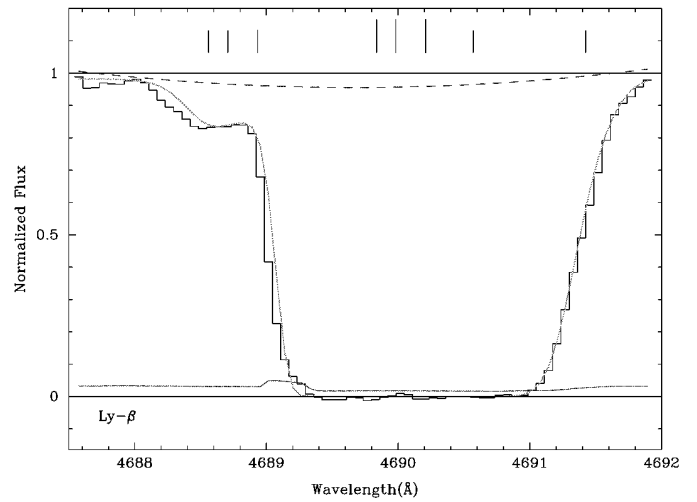


FIG. 2b

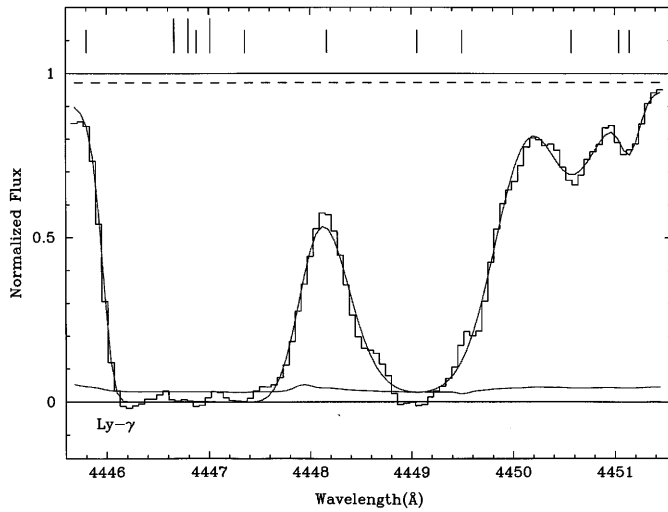


FIG. 2c

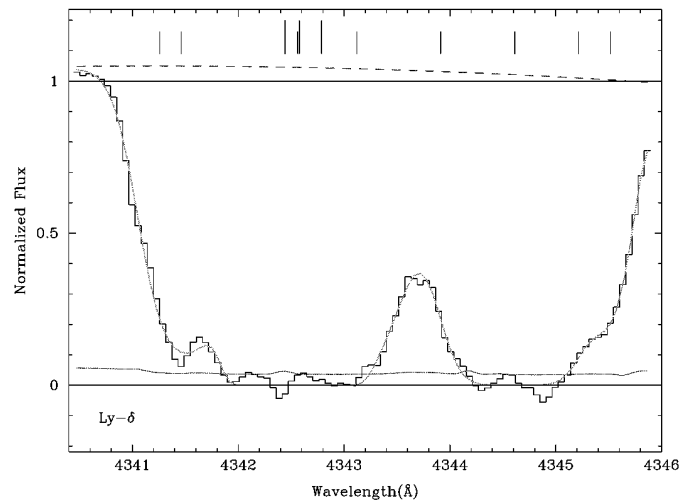


FIG. 2d

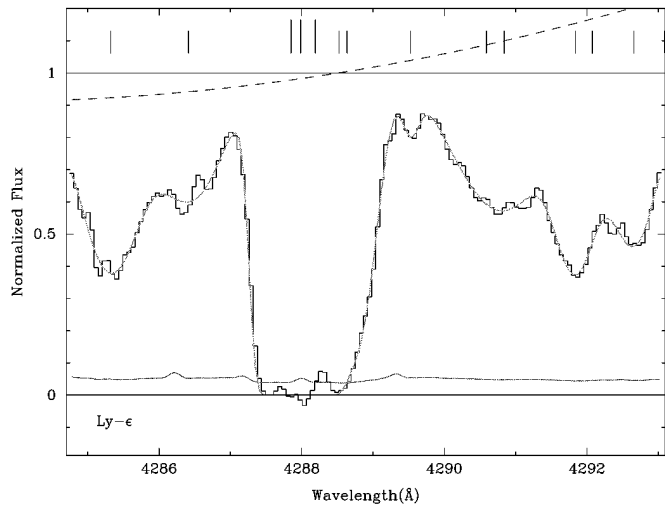


FIG. 2e

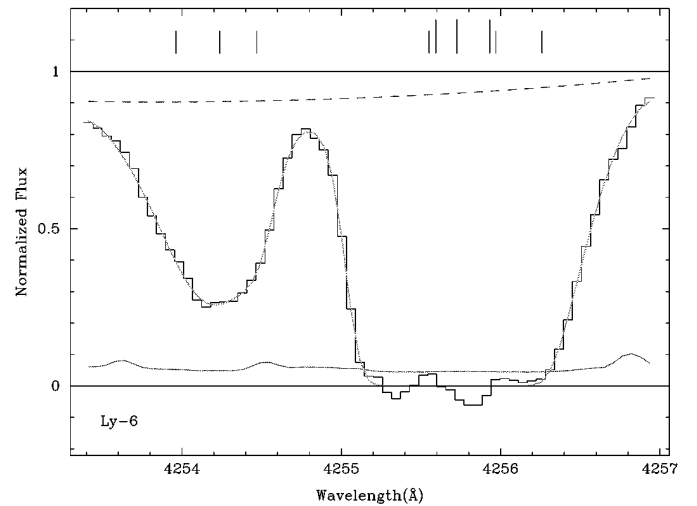


FIG. 2f

FIG. 2.—(a) Spectrum of the Ly α region of the DHAS. The data and model fit are displayed as in Fig. 1 representing the best fit of model 4. The dashed line shows a 5th order Legendre polynomial that gives the best fit to the unabsorbed QSO continuum. The tick marks show the positions of all absorbers that lie in each region. The taller tick marks show the three main hydrogen absorbers. The corresponding deuterium lines are located approximately 1 Å blueward of the hydrogen lines and are easily distinguishable with the same triple pattern. The solid line at unity represents our original estimate of the unabsorbed quasar continuum over the region. (b) Spectrum of the Ly β region of the DHAS. The continuum is a 3rd order Legendre polynomial. The gray line is the same model as in (a). (c) Same as (b), but for the Ly γ region of the DHAS. (d) Same as (b), but for the Ly δ region. (e) Same as (b), but for the Ly ϵ region. (f) Same as (b), but for the Ly6 region. (g) Same as (b), but for the Ly7 region. (h) Same as (b), but for the Ly9 region. (i) Same as (b), but for the Ly limit region.

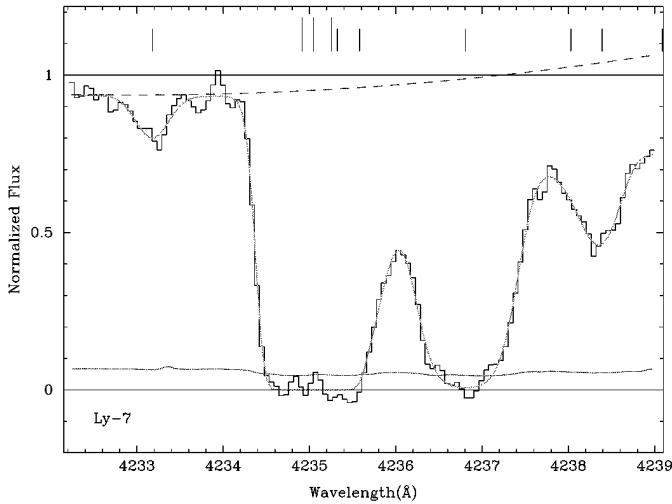


FIG. 2g

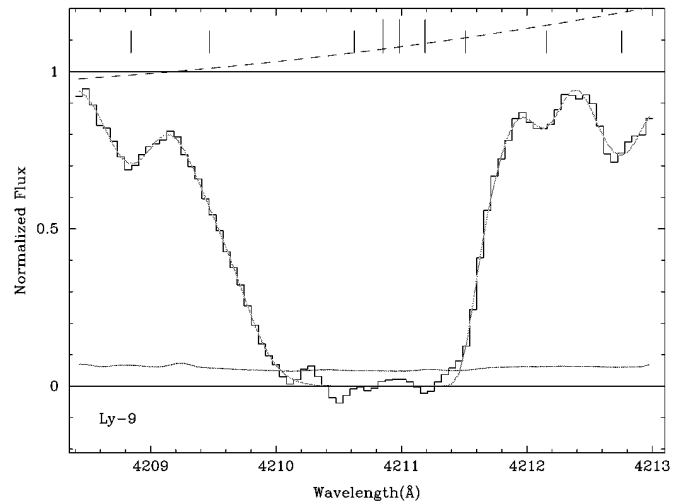


FIG. 2h

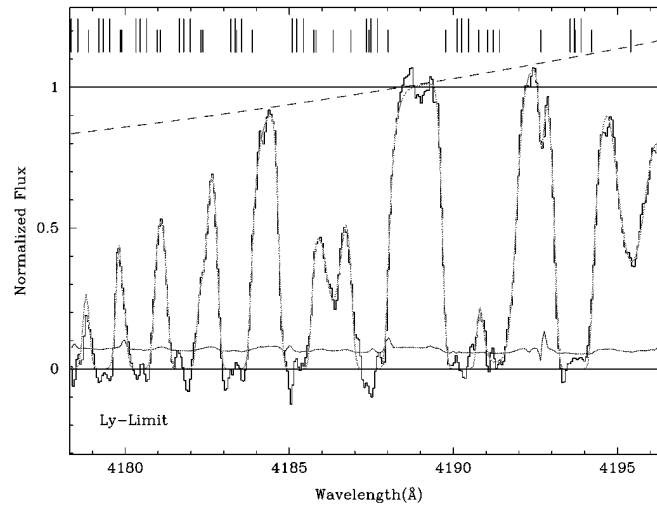


FIG. 2i

(Fig. 2, *dashed lines*). In the data reduction process, we use Legendre polynomials to normalize initially the spectrum to the regions of the spectrum showing no absorption (Fig. 2, *solid line* at unity). In the Ly α forest, the continuum is not well defined because of large regions of continuous absorption. We account for this uncertainty in the continuum in the Ly α forest by allowing the coefficients of the Legendre polynomials to be free parameters, without bounds, in our models. Therefore, the continuum is no longer fixed to the level on which we can only speculate. In statistical language, we fit the continuum level with a set of “nuisance parameters,” which we allow to vary freely to improve the fit because they are not of primary interest.

2.2.5. Regions of Interest

We must choose regions of the spectrum to compare to the models. If we model the entire Keck spectrum, the model would include over 1000 lines and over 40,000 pixels. For practical purposes, we can not model the entire spectrum simultaneously, as the time required to complete the fitting procedure scales as the number of lines times the number of pixels. Also, we want our model to be sensitive to D/H and not to other unrelated features in the spectrum. Therefore, we select regions of the spectrum that include at

least one Lyman series line of the DHAS. In principle, we want to include all Lyman series of the DHAS, but some Lyman series lines are blended with other strong, unassociated absorption lines and are not included in the selected regions.

In Figures 1 and 2, we show the regions of the spectrum used in the model fitting. Table 1 lists the regions used in our analysis, including the number of pixels and the order of the Legendre polynomial used to model the unabsorbed continuum in each region. The damping wings of the Ly α feature absorb over a large wavelength range; therefore, the span of the Ly α region is much greater than those of the other individual line regions. For the higher order Lyman lines, the regions of interest begin to overlap. The overlapping regions are combined into a single region containing multiple Lyman lines; this region is labeled the “Ly limit”.

2.2.6. Goodness of Fit to Different Spectral Regions

Of the nine regions, the Ly α region (Fig. 2a) has the highest signal-to-noise ratio (S/N) per pixel, approximately 75 per 4 km s $^{-1}$ pixel. Thus the entire fit is heavily weighted by Ly α , and the fit is most tightly constrained by the data in this region. Deuterium Ly α can be seen at 5557 Å and is composed of three components in the model presented here.

The fitted continuum contains five free parameters and is reasonably consistent with our initial estimate of the continuum. Only at the red edge does it begin to diverge significantly, and the overlap between the estimated and the best fit continua lies directly at the Ly α feature. The overlap in this region suggests that the new continuum determination will have little effect in the Ly α region.

The Ly β region (Fig. 2*b*) is much smaller than Ly α . The flux returns to the continuum much closer to the center of the Ly β line, and there is no reason to include a larger section around Ly β . Again, the best-fit continuum lies close to the original continuum estimate over the entire region. The model fit to Ly β is not as good as Ly α : there is underabsorption in two places near D Ly β . The blue wing of Ly β shows underabsorption, but there is a significant increase in the noise over some of these pixels ($4689.0 < \lambda < 4689.3$ Å), which is most likely caused by bad columns being rejected in the original CCD images. The underabsorption on the blueward side of D Ly β is likely caused by a hydrogen Ly α line (which is fit in model 7) that is blended with the deuterium feature. We label hydrogen lines that overlap and blend with the deuterium features “contaminating” hydrogen. Contamination will be discussed thoroughly in § 3.1 and introduced into our models 6 & 7.

The models must produce a good fit to all the Lyman lines simultaneously. We show each of the regions separately in Figure 2 to allow a close inspection of the data and model and to display how well the model reproduces the observed spectrum. Notice that there are additional absorbers overlapping the main components. These extra absorbers add free parameters to the fit and, in general, make the model less restrictive. That is, the parameters determining the main components cannot be as tightly constrained when overlapping absorbers are included.

In Figure 2*i*, we show the spectral region with the highest order Lyman lines, Ly12 to Ly19. The best-fit continuum shows a significant difference from the initial estimate. The unabsorbed continuum in this region was difficult to estimate because of the lack of pixels with little or no absorption. The continuum was originally estimated as a constant flux level passing near the few pixels with the highest flux. The large amount of absorption in this region did not allow for a better estimate of the unabsorbed continuum initially.

The difference between the best-fit continuum (*dotted line*) and the initial continuum (*solid line*) is likely caused by the simple approximation of the continuum level during the reduction. The shape of the best-fit continuum is more likely and is a function of the instrumental sensitivity in this region.

There are several regions of the spectrum shown in Figure 2 of TFB that have more flux than expected by their model fit. In the models presented here, this unabsorbed flux is accounted for with the extra hydrogen components and a different continuum.

3. RESULTS

Figure 3 shows the major results of the fitting procedure with the seven models. Table 3 summarizes the D/H measurements for each model. We performed the χ^2 minimization procedure for 100 values of D/H over the range $-4.95 < \log(D/H) < -4.0$ for each of the seven models.

For example, Figure 3*a* shows the results for the two-component model (model 1). The solid dark gray line represents one of the components and the dashed line

represents the other. These graphs show the behavior of the main component parameters as a function of D/H. The parameters sometimes display discontinuous behavior, which is caused by the nonuniqueness of Voigt profile fitting. The χ^2 minimization has found two equally likely solutions, and this exhibits itself with a discontinuous change in the parameter values. Although the fitted parameters may be nonunique, χ^2_{\min} remains a smooth function of D/H. The exact parameters that give the best fit are not well determined, but the χ^2_{\min} and the D/H are well defined. In this analysis, we cannot attempt to model the DHAS exactly, but we can still find the relative likelihood for all values of D/H.

We cannot model the individual components exactly because of the intrinsic blending of the absorption lines, but we do find that parameters that include all the components can be measured precisely. In Figure 3, the thick solid line in the column density plot represents the total neutral hydrogen column, $N(\text{H I})_{\text{total}}$. This is merely the sum of the column densities of all components in a given model at a specific value of D/H. We find that all seven models give an $N(\text{H I})_{\text{total}}$ that is a smooth function of D/H, even though the individual column densities in the models are not. $N(\text{H I})_{\text{total}}$ is the quantity subject to the constraint provided by Burles & Tytler (1997), $N(\text{H I})_{\text{total}} = 17.86 \pm 0.02$. For a model that gives an arbitrarily good fit to the spectral regions, the best fit will depend only on the agreement with the $N(\text{H I})_{\text{total}}$ constraint.

We can measure D/H directly from Figure 3. With a χ^2 function of one variable, the confidence levels are easily determined. The 95% confidence levels correspond to $\Delta\chi^2 = 4.0$, where $\Delta\chi^2 = \chi^2 - \chi^2_{\min}$. For each model in Figure 3, we find the minimum of the χ^2 function and list this value in Table 3. The 95% confidence levels on D/H are also listed in Table 3 and are shown as vertical dashed lines in Figure 3. The fitting procedure is not perfect, and we can see in Figure 3 that there are deviations from perfectly smooth χ^2 functions.

The fitting procedure can converge before reaching the absolute minimum χ^2 , and we estimate that the difference between the absolute minimum and the calculated χ^2 can be as large as 0.5. We take this deficiency into account by setting the 95% confidence levels at $\Delta\chi^2 = 4.5$.

All of the regions of 95% confidence in Figure 3 overlap with the central value of $N(\text{H I})_{\text{total}}$ constraint. The best-fit model of D/H must not only provide the best fit to the spectral regions but must also fit the constraint of $N(\text{H I})_{\text{total}}$. For all models, the values of $N(\text{H I})_{\text{total}}$ decrease smoothly with increasing D/H. $N(\text{D I})$ is tightly constrained by D Ly α and D Ly β , so as D/H increases, $N(\text{H I})$ must decrease, which gives smoothly varying functions of $N(\text{H I})_{\text{total}}$ for each model. In all models, the 95% confidence regions on D/H represent the model fits where the $N(\text{H I})_{\text{total}}$ constraint is well satisfied.

All seven models give consistent ranges for the 95% confidence regions, as seen in Figure 4. As expected, the models with more free parameters have larger confidence regions. Except for model 6, which includes hydrogen contamination at Ly α , all models are consistent with

$$\log(D/H) = -4.49 \pm 0.04 \quad (1)$$

or

$$(D/H) = 3.24 \pm 0.30 \times 10^{-5} \quad (2)$$

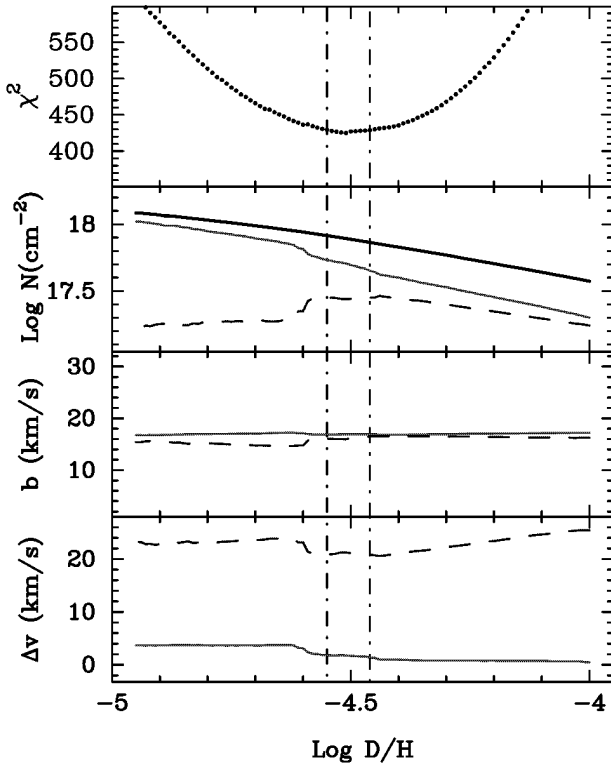


FIG. 3a

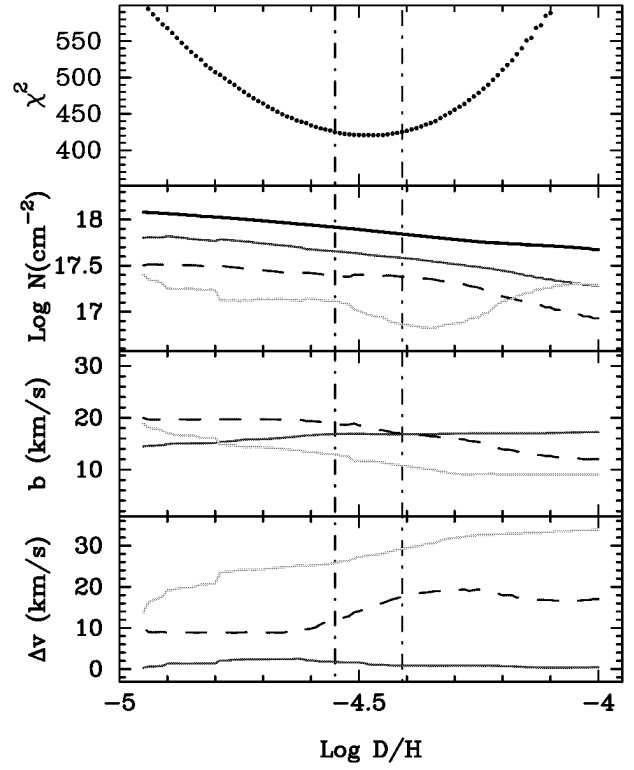


FIG. 3b

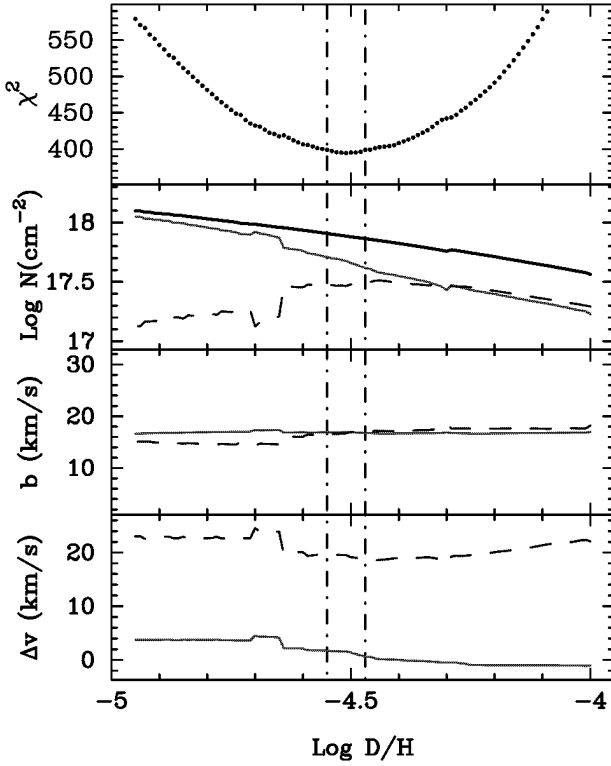


FIG. 3c

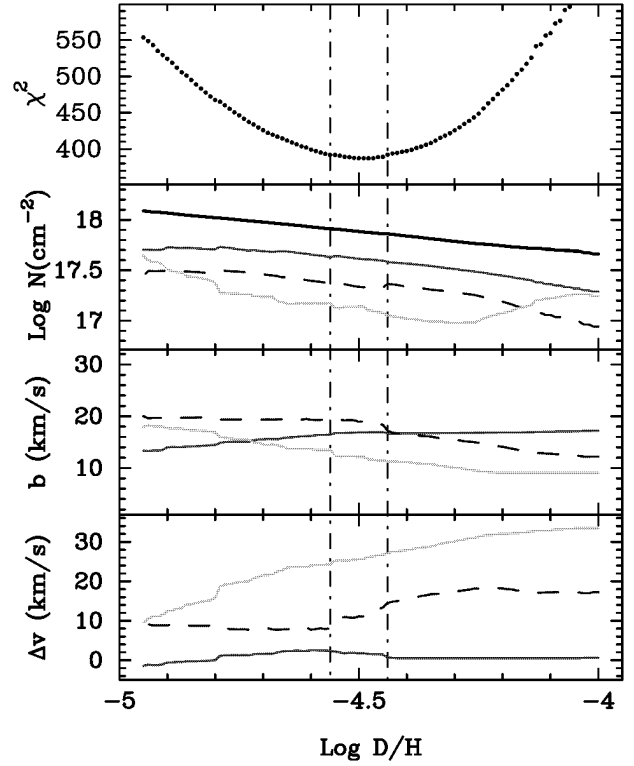


FIG. 3d

FIG. 3.—(a) Results of the fitting procedure for model 1. The top panel shows χ^2_{\min} as a function of $\log(D/H)$. The remaining panels show N , b , and z that give the best fit for the main H I components. The parameters are represented as thin lines with different line styles for each component. The bottom panel shows the relative velocity positions of the two components; $\Delta v = 0$ corresponds to $z = 3.572201$. (b) Same as (a), but for model 2 with three components. (c) Same as (a), but for model 3 with two components. (d) Same as (a), but for model 4 with three components. (e) Same as (a), but for model 5 with four components. (f) Same as (a), but for model 6 with three components and contamination at D Ly α . (g) Same as (a), but for model 7 with three components and contamination at D Ly β .

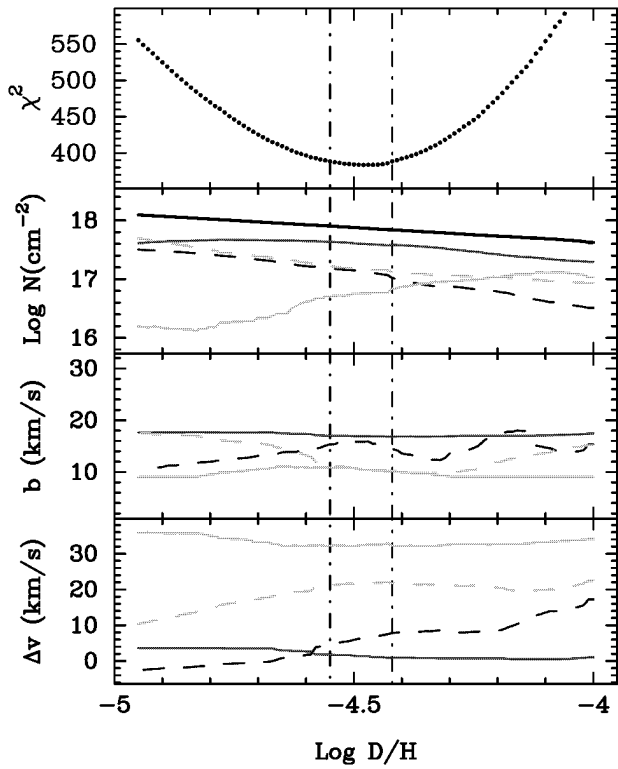


FIG. 3e

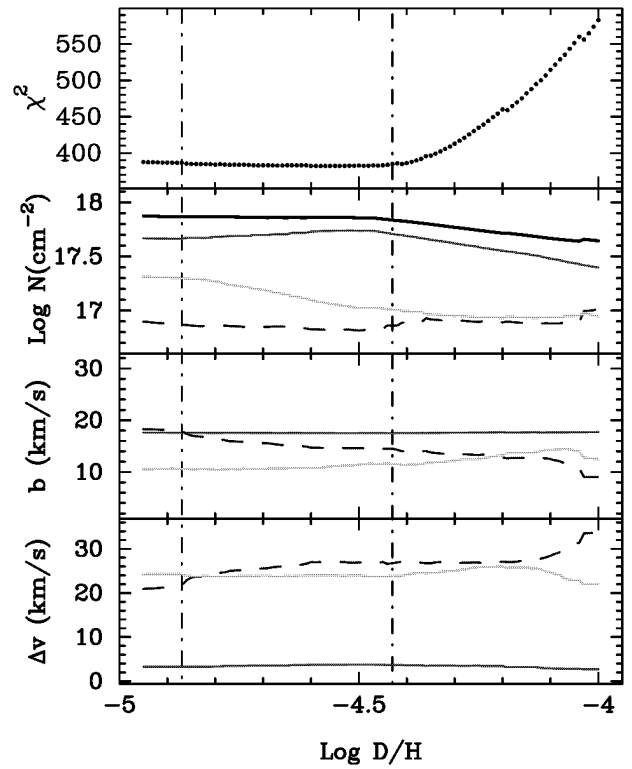


FIG. 3f

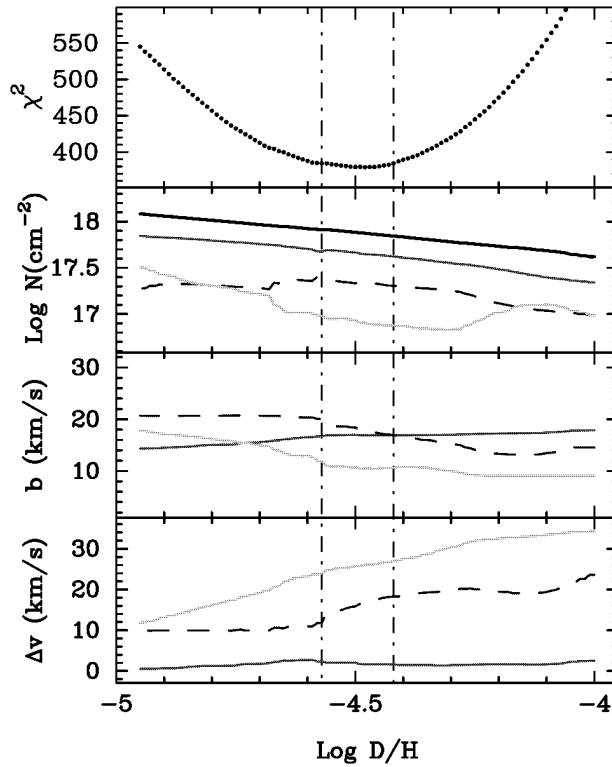


FIG. 3g

at 67% confidence. The shape of the χ^2_{\min} functions indicate errors that are normally distributed in $\log(D/H)$, and the 67% confidence levels should be one-half of the 95% levels.

3.1. Contamination

In models 6 & 7, we investigate the effects of hydrogen contamination of the D Lyman lines. Model 6 includes an

additional hydrogen absorber at redshift $z = 3.5710$, which places its lines near the deuterium lines. Figure 3f shows the results of the fitting procedure. For values of $\log D/H > -4.5$, the results are identical to model 4, which did not include contamination, but for lower values of D/H , the contaminating hydrogen absorbs a significant amount of flux at the D Ly α and D Ly β lines and gives a good fit by

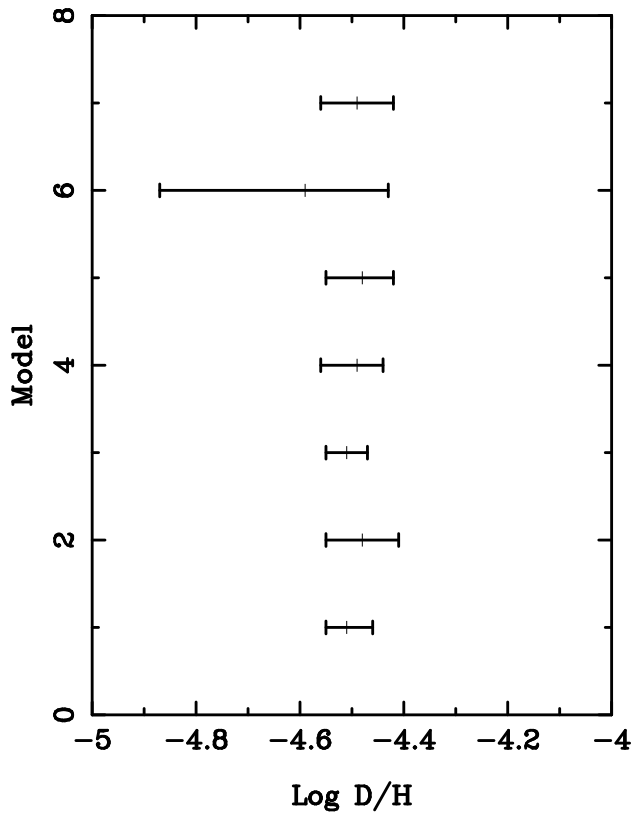


FIG. 4.—95% confidence regions of D/H for the seven models in Table 3. The central vertical tick marks show the values of D/H that gave the best fit in each model.

keeping $N(\text{H I})_{\text{total}}$ nearly constant and lowering $N(\text{D I})$. Although contamination allows for lower D/H as expected, the introduction of an additional Ly α absorber with three free parameters does not improve the fit significantly. This result is in sharp contrast to another D/H system, toward Q1009 + 2956, where contamination significantly improves χ^2 (Burles & Tytler 1998). We conclude that Ly α contamination is not significant in this D/H system for two reasons: (1) additional parameters for contamination do not improve the χ^2 fit, and (2) the likelihood of significant contamination drawn from distributions of the Ly α forest (Kirkman & Tytler 1997; Lu et al. 1997) is small (see Tytler & Burles 1997; TFB; Jedamzik & Fuller 1997; Steigman 1994).

Model 7 includes contamination at the position of D Ly β , at $z = 2.8565$. This redshift is much lower than the DHAS, and the hydrogen absorber affects only D Ly β . The extra absorber is initially placed at the center of D Ly β and is allowed to move freely to achieve the best fit to the data. The fit improves by $\Delta\chi^2 \approx 7.0$ as the hydrogen absorber fills in the underabsorption seen in Figure 2b. The best fit for model 7 is shown in Figure 5, and the improvement is easily seen upon comparison with Figure 2b. The model shows under absorption in 3 pixels near 4689 Å (-60 km s^{-1} blueward of H Ly β), but these pixels fall in a region of spectra with increased noise. In conclusion, we find that model 7 is consistent with the results from the other models that did not include this contamination and that the measurement of D/H is robust with any extra hydrogen absorption at Ly β alone.

The presence of contamination will give an overestimate of D/H. Therefore, the upper limit on D/H is robust and not

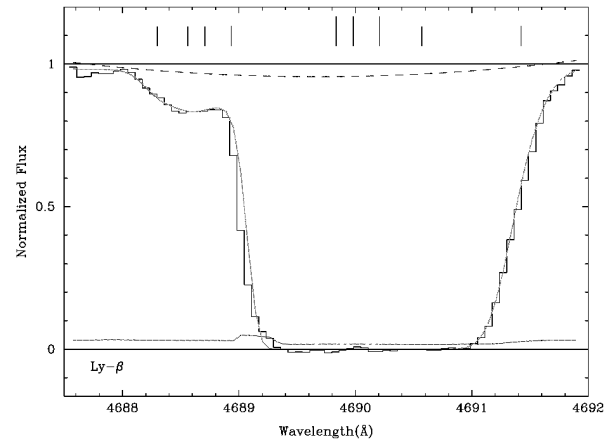


FIG. 5.—Same as Fig. 2b, but with the best fit for model 7

affected by the presence of contamination. All seven models are consistent with the upper limit, $D/H < 3.9 \times 10^{-5}$.

4. IONIZATION AND METALS

The metal absorption lines associated with the DHAS were analyzed by TFB. We use the two-component fit ($z = 3.572201, 3.572428$) of TFB to measure the column densities of the ions shown in Table 4. If no feature is detected at the expected positions of the ionic transitions, then we place a 2σ upper limit on the total column density. More absorption components could be used to describe the metal lines in this DHAS, but the qualitative results will remain unchanged. We used the program CLOUDY (Ferland 1996) with an ionizing background spectrum calculated by Haardt & Madau (1996) to calculate the ionization state of the gas in each component. Table 5 shows the metallicity, temperature, ionization parameter, and total hydrogen density in each component calculated from the CLOUDY simulations.

The equilibrium temperatures calculated from the CLOUDY simulations can be directly compared to the temperatures determined from the velocity dispersions of the H, C, and Si lines. In the blue component, we find a good agreement between the temperatures shown in Table 4, but, in the red component, the CLOUDY equilibrium temperature is smaller than the temperature determined

TABLE 4
COLUMN DENSITIES OF METALS

Species	Blue Component	Red Component
C I		$< 12.4 (2\sigma)$
C II	12.70 ± 0.08	13.27 ± 0.03
C III	13.36 ± 0.09	13.82 ± 0.19
C IV	12.22 ± 0.16	12.61 ± 0.11
N I		$< 12.6 (2\sigma)$
N II		$< 13.9 (2\sigma)$
N III ^a	13.15 ± 0.71	13.84 ± 0.39
N V		$< 12.4 (2\sigma)$
O I		$< 12.6 (2\sigma)$
Si II	11.76 ± 0.07	12.41 ± 0.02
Si III	12.73 ± 0.20	13.20 ± 0.05
Si IV ^b	12.12 ± 0.12	13.01 ± 0.02
Fe II	11.58 ± 0.44	12.41 ± 0.10
Fe III	12.83 ± 0.58	13.30 ± 0.10

^a Absorption feature is blended in Ly α forest.

^b Si IV $\lambda 1393$ is blended with C IV $\lambda 1550$ at $z = 3.1097$.

TABLE 5
METALLICITY AND IONIZATION STATE OF DHAS

Parameter	Blue Component	Red Component
[C/H]	−3.0	−2.1
[N/H]	≤ −2.7	≤ −2.0
[O/H]	< −0.9	< −0.9
[Si/H]	−2.7	−1.9
[Fe/H]	< −1.5	< −0.6
log U	−2.9	−3.0
log H I/H	−2.35	−2.29
log n_{H}^{a} (cm $^{-3}$)	−1.70	−1.60
L (kpc)	1.5	0.6
T_{b}^{b}	1.62 ± 0.09	2.36 ± 0.09
T_{e}^{c}	1.72	1.67
$b_{\text{tur}}^{\text{c}}$	4.8 ± 0.8	8.4 ± 0.4

^a Corresponding to log $J_0 = -21.3$.

^b Determined from component line widths.

^c Photoionization equilibrium temperature.

from the relative line widths, including b_{tur} . This may indicate another component near the velocity position of the red component. The CLOUDY simulations did not give an acceptable fit to all ions of Si in the red component. A single phase of photoionization could not account for the three column densities observed, and the calculated $[\text{Si}/\text{H}]_{\text{red}}$ came from Si II and Si III alone. We excluded Si IV for two reasons: (1) Si IV $\lambda 1393$ is blended with C IV $\lambda 1550$ at $z = 3.1097$, and (2) it is likely that there is another component of higher ionization that contributes to Si IV.

We have not attempted to model the metal lines with more than two components. Although the column densities of the individual components would differ, the derived metallicities of the components would not greatly differ from the results shown in Table 5. All components would have metallicities below 1/100 solar, independent of the model used.

We can now test the TFB assumption that the H and D lines were at the velocities of the C and Si metal lines. In general, this assumption adds a systematic error to the measurement if the metal lines are not aligned with the H I and D I lines. This DHAS is rather unique because all the metal lines, with different ionizations, show similar velocity structures. In Figure 3, the velocity positions of the blue and red components used by TFB lie at $\Delta v = 0$ and 15 km s^{-1} , respectively. In our models with three or four components, two of the components lie near the velocity positions of the metal lines, with considerable variation, depending on D/H, but in the two-component models, the component separation for the most likely D/H is 19 km s^{-1} , rather than 15 km s^{-1} , and the red hydrogen component is at a higher velocity position for all values of D/H. This shows that a systematic offset in the red component was introduced in the analysis in TFB by assuming that the H and D lines fell precisely at the metal line positions in the two-component model. It is difficult to translate this velocity offset into a D/H change because, as seen in Figure 3, many other coupled parameters are involved.

5. PRIMORDIAL D/H

We have measured the deuterium abundance in the DHAS at $z = 3.5722$ toward Q1937–1009. Within the statistical uncertainties, we conclude that this is the primordial value of D/H produced by big bang nucleosynthesis (Reeves et al. 1973; Epstein et al. 1976). This absorption system is

young ($\leq 1 h^{-1} \text{ Gyr}$) and very metal poor ($[\text{X}/\text{H}] \leq -2.0$). These characteristics place strong constraints on stellar astration of deuterium independent of initial mass functions and star formation rates (Jedamzik & Fuller 1997; Fields 1996). To astrate significant amounts of deuterium, high-mass stars would overproduce CNO and Si, and low-mass stars would not have time to complete their evolution. With no post-BBN processes to create or destroy deuterium, our measured value of D/H must represent the primordial value.

5.1. Other D/H Measurements

Because of its importance in the standard cosmological model, D/H has been measured in many astrophysical sites. In the local interstellar medium, Piskunov et al. (1997) find a mean abundance ratio, $\text{D}/\text{H}_{\text{ISM}} = 1.6 \pm 0.2 \times 10^{-5}$, in the lines of sight toward nearby stars. Chengalur, Braun, & Burton (1997) have recently detected the D I hyperfine transition in emission toward the Galactic anticenter and find $\text{D}/\text{H} = 3.9 \pm 1.0 \times 10^{-5}$. Abundance measurements in meteorites, the lunar soil, and the atmospheres of the Jovian planets are consistent with a presolar value, $\text{D}/\text{H}_{\odot} = 2.6 \pm 1.0 \times 10^{-5}$ (Gautier & Owen 1983; Geiss 1993; Encrenaz et al. 1996). In the next section, we use the local measurements of D/H with our measurement at high redshift to discuss the evolution of D/H.

Tytler & Burles (1997) have made another measurement of D/H in a high-redshift Lyman limit system toward Q1009+2956 at $z = 2.504$. Preliminary analysis of this object gives $\text{D}/\text{H} = 3.0 \pm 0.6 \times 10^{-5}$, and simulations of hydrogen contamination suggest that the most likely value is $\text{D}/\text{H} = 2.5 \pm 0.5 \pm 0.4 \times 10^{-5}$ (statistical and systematic error). The measurement toward Q1009+2956 agrees very well with the result obtained in this paper toward Q1937–1009. An analysis of Q1009+2956 with the methods presented here will be presented in Burles & Tytler (1998).

There have been other reports of deuterium detections in high-redshift QSO absorption systems toward Q0014+8118 (Songaila et al. 1994; Carswell et al. 1994; Rugers & Hogan 1996a, 1996b), toward Q1202–0725 (Wampler et al. 1996), and toward Q0420–388 (Carswell et al. 1996). These other systems do not yield measures of D/H because of either lower quality spectral data or greater complexities in the velocity structure of the absorption system. The next best candidate system to measure D/H, at $z = 3.32$ toward Q0014+8118, was shown to have an interloping hydrogen cloud within 10 km s^{-1} of the expected position of deuterium (Tytler, Burles, & Kirkman 1998). Webb et al. (1997) recently deduced a D/H value at $z = 0.701$ toward the low-redshift QSO 1718+4807 using a spectrum obtained with the *Hubble Space Telescope* (HST). Unlike Q1937–1009 and Q1009+2656, only one H I line was observed, so the velocity structure of H I is not well known. Assuming a single component fit to the Ly α , they find $\text{D}/\text{H} = 20 \pm 5 \times 10^{-5}$, but this value will remain suggestive unless confirmed with approved HST observations of the high-order Lyman lines.

5.2. Chemical Evolution of Deuterium

Many groups have discussed the significance of deuterium in galactic chemical evolution and have used simple models to calculate the abundance ratio, D/H, as a function of time and metallicity (Clayton 1985; Audouze & Tinsley

1974; Steigman & Tosi 1992; Edmunds 1994; Vangioni-Flam, Olive, & Prantzos 1994; Steigman & Tosi 1995; Prantzos 1996; Fields 1996; Scully et al. 1997). In the past, deuterium evolution was required in order to extrapolate the ISM and presolar nebula measurements of D/H back in time, and back to zero metallicity, to constrain the primordial D/H value. However, now the problem can be inverted: we can use the values of primordial D/H, presolar D/H, and the ISM D/H to constrain models of chemical evolution, deuterium astration as a function of time and metallicity, and the fraction of baryons that have been cycled through stars in the solar neighborhood. The ratio of the ISM and primordial values gives an astration factor in the local ISM of

$$d = \frac{(D/H)_{\text{ISM}}}{(D/H)_p} = 0.5 \pm 0.05. \quad (3)$$

Therefore, we can make the simple statement that one-half of the gas in the local ISM has been cycled through stars. This fraction can be used to place new limits on the stellar initial mass function and the amount of inflow and/or outflow in the local ISM. When one considers published models of chemical evolution in the ISM, the amount of deuterium astration agrees well with models incorporating standard star formation and some infall of primordial material (Edmunds 1994; Clayton 1985; Fields 1996).

5.3. The Baryon Density

Production of the light elements from standard big bang nucleosynthesis (SBBN) depends on a single parameter, η , the baryon-to-photon ratio during SBBN. Many groups have calculated the abundance yields of the light elements as a function of η (Wagoner et al. 1967; Walker et al. 1991; Smith et al. 1993; Krauss & Kernan 1995; Copi et al. 1995). The abundance yield of deuterium is a single-valued function of η , and using output from the Kawano BBN code (Kawano 1992), we find

$$\eta = 5.3 \pm 0.3 \pm 0.25 \times 10^{-10}, \quad (4)$$

where the first error is the statistical uncertainty in the D/H measurement and the second error represents the statistical uncertainty in the nuclear cross sections (Smith et al. 1993). It is interesting to note that the magnitude of the measurement errors are comparable to the errors in the SBBN calculations.

If we use the present-day photon density determined from the *COBE* Far-Infrared Absolute Spectrometer (FIRAS) measurements of the cosmic microwave background (CMB; Fixsen et al. 1996), we can directly calculate the present-day baryon density

$$\Omega_b h^2 = 0.0193 \pm 0.0014, \quad (5)$$

where the error includes both uncertainties in η . This value for the baryon density agrees with recent estimates of $\Omega_b h^2$ from observations of the CMB power spectrum, the intergalactic medium at $z \approx 3$, and rich galaxy clusters at $z \approx 0.3$.

The power spectrum of anisotropies in the CMB determines Ω_b at the epoch of decoupling, $z \approx 1000$ (Hu & White 1996). The locations and heights of the Doppler peaks in the CMB power spectrum provide constraints on Ω_b . The current observational state of the CMB power spectrum does not have the precision to determine Ω_b , although there are hints of the first Doppler peak and statistical analyses

suggest $\Omega_b < 0.28$, consistent with SBBN (Lineweaver et al. 1997). Future CMB experiments, including the *Microwave Anisotropy Probe* and *Planck* satellites, promise to determine Ω_b to 2%, which will provide an independent check on our measurement and a consistency test for SBBN.

At redshifts $z < 5$, the intergalactic medium (IGM) is ionized and can be observed through absorption in high-redshift QSO spectra. Recent comparisons of high-resolution spectroscopy of the IGM and large cosmological simulations require a high baryon density to account for the observed Ly α forest, $\Omega_b \geq 0.017 h^{-2}$ (Rauch et al. 1997; Weinberg et al. 1997; Zhang et al. 1997). Other estimates include the baryons in protogalaxies seen in damped Ly α absorption with $\Omega_{\text{damped}} \approx 0.002 h^{-1}$ (Wolfe et al. 1995) and the baryons in the diffuse IGM that are not seen in Ly α absorption, $0.0001 h^{-1} < \Omega_{\text{diff}} < 0.007 h^{-3/2}$ (Reimers et al. 1997). The inventory of baryons at $z \approx 3$ demands a high cosmological baryon density consistent with our measurements of D/H.

At low redshift, only a small fraction ($\approx 10\%$) of the baryons reside in stars and visible gas, with estimates ranging from $\Omega_* \approx 0.003 - 0.007 h^{-1}$ (Persic & Salucci 1992), but a fair sample of today's baryons are likely to be in gas heated through supernova explosions or accretion into the large potential wells of galaxy clusters. A recent application of Oort's method to 14 fields containing rich galaxy clusters yields a baryon density in the form of hot gas, $\Omega_{\text{gas}} \approx 0.012 - 0.016 h^{-3/2}$ (Carlberg et al. 1998). This result is valid assuming that the baryons and emitted light trace the total matter density and that clusters provide a fair sample of the baryon fraction. If most of the baryons today are in the form of hot gas, they must be collisionally ionized (Giallongo, Fontana, & Madau 1997) and could have already been detected in a survey for O VI at $z \approx 0.9$ (Burles & Tytler 1996).

Measurements of the total cosmological matter density Ω_m imply that baryons cannot constitute all the matter in the universe. A number of methods have been used to estimate Ω_m (see Dekel, Burstein, & White 1996). Peculiar velocities of galaxies can be treated as cosmic flows induced by large-scale mass distributions. In particular, cosmic flows in large-scale voids places a lower limit on the total mean matter density, $\Omega_m > 0.3$ (Dekel 1997). This limit on Ω_m places an upper limit on the baryon fraction, $f_b < 0.07$, which agrees with the fraction inferred from X-ray observations of galaxy clusters (White et al. 1993; White & Fabian 1995; Lowenstein et al. 1996; Myers et al. 1997) and groups (Mulchaey et al. 1996), as well as Sunyaev-Zeldovich measurements toward galaxy clusters (Myers et al. 1997).

5.4. Other Light Elements

In SBBN, the determination of η implies the primordial abundance ratios for the other light elements. We now use our D/H measurement to infer the primordial abundances of the other light elements. In the following, we use the output from the Kawano Code with $\tau = 887$ s, and $N_\nu = 3.0$. All errors are 67% confidence and include the uncertainties in the nuclear cross sections and neutron lifetime. Our measurement infers a primordial ${}^4\text{He}$ mass fraction Y_p of

$$Y_p = 0.247 \pm 0.002. \quad (6)$$

The comparison between D and ${}^4\text{He}$ provides a crucial test of SBBN (Cardall & Fuller 1996; Hata et al. 1997), but

recent measurements of the ^4He abundance in extragalactic metal-poor H II regions have given discrepant results. Izotov, Thuan, & Lipovetsky (1997a, 1997b) compiled a homogeneous sample of 45 H II regions taken mainly from the Second Byurakan Survey (see Izotov et al. 1993) and found $Y_p = 0.243 \pm 0.003$ (Izotov et al. 1997a, 1997b), which is consistent with the value of Y_p we infer. On the other hand, Olive, Skillman, & Steigman (1997) have compiled a large sample of H II regions from studies by Olive & Steigman (1995), Izotov et al. (1994), and Izotov et al. (1997a, 1997b) and obtain $Y_p = 0.234 \pm 0.002$, which is consistent with neither Izotov et al. (1997a, 1997b) nor our inferred value. The differences in the two ^4He studies must be properly understood before a direct comparison can be made between D and ^4He . Olive et al. (1997) argue that the difference can be entirely accounted for in the atomic data sets and the lowest metallicity region, IZw 18. Skillman & Kennicutt (1993) observed IZw 18 and found $Y = 0.231 \pm 0.005$. Izotov & Thuan (1997) reobserved IZw 18, and they infer $Y = 0.243 \pm 0.009$. The different results obtained for this H II region highlights the uncertainties in the current observational determinations of Y_p .

The primordial value of D/H infers an abundance for ^7Li ,

$$A(\text{Li}) = 2.5 \pm 0.17, \quad (7)$$

where $A(\text{Li}) = 12 + \log(\text{Li}/\text{H})$. The abundance of ^7Li observed in the Spite “plateau” of warm metal-poor halo stars (Spite & Spite 1982; Spite, Maillard, & Spite 1984; Rebolo, Beckman, & Molaro 1988; Thorburn 1994; Bonifacio & Molaro 1997) is lower but consistent with the inferred ^7Li from D/H. Bonifacio & Molaro have recently analyzed a large sample of suitable halo stars using infrared measurements to give a better indication of effective temperatures. They find $A(\text{Li}) = 2.238 \pm 0.012 \pm 0.05$ (statistical and systematic errors; Bonifacio & Molaro 1997) and no evidence for a dispersion in the plateau abundances, nor do they find correlations of $A(\text{Li})$ with effective temperature or metallicity. Our D/H measurements are consistent with the ^7Li abundance found by Bonifacio & Molaro (1997), but large errors in nuclear reaction rates required in the BBN simulations also allow for nonstandard depletion mechanisms in halo stars, which could have lowered the

plateau by as much as 0.6 dex (Pisonneault, Deliyannis, & Demarque 1992; Vauclair & Charbonnel 1995).

There do not exist any convincing measurements of a primordial ^3He abundance, although great efforts have been made to measure ^3He in Galactic H II regions (Balsler et al. 1994) and planetary nebulae (Balsler et al. 1997) using the hyperfine radio line. Stars can both produce or destroy ^3He , so any attempts to infer the primordial abundance of ^3He from galactic measurements are dominated by uncertainties in the chemical evolution of ^3He (Galli et al. 1995). If we look at the other side of the problem, we can use our inferred primordial value

$$\frac{^3\text{He}}{\text{H}} = 1.2 \pm 0.2 \times 10^{-5} \quad (8)$$

to study the chemical evolution of ^3He .

With the current state of the observations of the light elements and the associated uncertainties with inferring primordial abundances, we conclude that there is no inconsistency between deuterium and the other light elements with the predictions from SBBN. Furthermore, the determination of η with predictions from SBBN should be heavily weighted toward measurements of D/H in QSO absorption systems (Fuller & Cardall 1996; Schramm & Turner 1998).

We are extremely grateful to the W. M. Keck foundation, which made this work possible, to Steve Vogt and his team for building HIRES, to Judy Cohen, Bev Oke, and their team for building the Low-Resolution Imaging Spectrometer, and to Tom Bida, Randy Campbell, and Wayne Wack for assistance at the telescope. We are very grateful to Joseph Miller and the staff of Lick Observatory for the construction and maintenance of and assistance with the Kast spectrograph, which was made possible by a generous gift from William and Marina Kast. We thank Christian Cardall, George Fuller, Karsten Jedamzik, David Kirkman, Martin Lemoine, and Jason X. Prochaska for many useful conversations. D. T. thanks the European Southern Observatory for kind hospitality. This work was supported by NASA grant NAG 5-3237 and NSF grant AST 94-20443.

REFERENCES

- Adams, T. F. 1976, *A&A*, 50, 461
 Audouze, J., & Tinsley, B. 1974, *ApJ*, 192, 487
 Balsler, D. S., Bania, T. M., Brockway, C. J., Rood, R. T., & Wilson, T. L. 1994, *ApJ*, 430, 667
 Balsler, D. S., Bania, T. M., Rood, R. T., & Wilson, T. L. 1997, *ApJ*, 483, 320
 Bonifacio, P., & Molaro, P. 1997, *MNRAS*, 285, 847
 Burles, S. 1998, in preparation
 Burles, S., & Tytler, D. 1996, *ApJ*, 460, 584
 ———, 1997, *AJ*, 114, 1330
 ———, 1998, *ApJ*, submitted
 Cardall, C. Y., & Fuller, G. M. 1996, *ApJ*, 472, 435
 Carlberg, R. G., et al. 1998, *ApJ*, submitted
 Carswell, R. F., Rauch, M., Weymann, R. J., Cooke, A. J., & Webb, J. K. 1994, *MNRAS*, 268, L1
 Carswell, R. F., et al. 1996, *MNRAS*, 278, 506
 Chengalur, J. N., Braun, R., & Burton, W. B. 1997, *A&A*, 318, L35
 Clayton, D. D. 1985, *ApJ*, 290, 428
 Copi, C. J., Schramm, D. N., & Turner, M. S. 1995, *Science*, 267, 192
 Dekel, A. 1997, in *Formation of Structure in the Universe*, ed. A. Dekel & J. P. Ostriker (Cambridge: Cambridge Univ. Press)
 Dekel, A., Burstein, D., & White, S. D. M. 1996, preprint
 Edmunds, M. G. 1994, *MNRAS*, 270, L37
 Encenaz, T. 1996, *A&A*, 315, 397
 Epstein, R. I., Lattimer, J. M., & Schramm, D. N. 1976, *Nature*, 268, 198
 Ferland, G. J. 1996, HAZY, a Brief Introduction to CLOUDY, Univ. Kentucky Dept. Phys. Internal Report
 Fields, B. 1996, *ApJ*, 456, 478
 Fixsen, D. J., Cheng, E. S., Gales, J. M., Mather, J. C., Shafer, R. A., & Wright, E. L. 1996, *ApJ*, 473, 576
 Fuller, G. M., & Cardall, C. Y. 1996, *Nucl. Phys. B*, 51, 71
 Galli, D., Palla, F., Ferrini, F., & Penco, U. 1995, *ApJ*, 443, 536
 Gautier, D., & Owen, T. 1983, *Nature*, 304, 691
 Geiss, J. 1993, in *Origin and Evolution of the Elements*, ed. N. Prantzos, E. Vangioni-Flam, & M. Casse (Cambridge: Cambridge Univ. Press), 89
 Giallongo, E., Fontana, A., & Madau, P. 1997, *MNRAS*, 289, 629
 Haardt, F., & Madau, P. 1997, *ApJ*, 461, 20
 Hata, N., Steigman, G., Bludman, S., & Langacker, P. 1997, *Phys. Rev. D*, 55, 540
 Hu, W., & White, M. 1996, *ApJ*, 471, 30
 Ikeuchi, S., & Ostriker, J. P. 1986, *ApJ*, 301, 522
 Izotov, Yu. I., Lipovetsky, V. A., Guseva, N. G., Kniazev, A. Yu., Neizvestny, S. I., & Stepanian, J. A. 1993, *Astron. Astrophys. Trans.*, 3, 193
 Izotov, Y. I., & Thuan, T. X. 1997, preprint
 Izotov, Y. I., Thuan, T. X., & Lipovetsky, V. A. 1994, *ApJ*, 435, 647
 ———, 1997a, *ApJ*, 435, 647
 ———, 1997b, *ApJS*, 108, 1
 Jedamzik, K., & Fuller, G. M. 1997, *ApJ*, 483, 560
 Kawano, L. 1992, preprint
 Kirkman, D., & Tytler, D. 1997, *ApJ*, 484, 848
 Krauss, L. M., & Kernan, P. J. 1995, *Phys. Lett. B*, 347, 347
 Lineweaver, C. H., Barbosa, D., Blanchard, A., & Bartlett, J. G. 1997, *A&A*, 322, 365

- Lowenstein, M., & Mushotzky, R. F. 1996, *ApJ*, 471, L83
- Lu, L., Sargent, W. L. W., Womble, D. S., & Takada-Hidai, M. 1997, *ApJ*, 472, 509
- Mulchaey, J. S., Davis, D. S., Mushotzky, R. F., & Burstein, D. 1996, *ApJ*, 456, 80
- Myers, S. T., Baker, J. E., Readhead, A. C. S., Leitch, E. M., & Herbig, T. 1997, *ApJ*, 485, 1
- Olive, K. A., Skillman, E. D., & Steigman, G. 1997, *ApJ*, 483, 788
- Olive, K. A., & Steigman, G. 1995, *ApJS*, 97, 49
- Persic, M., & Salucci, P. 1992, *MNRAS*, 258, 14
- Pisonneault, M. H., Deliyannis, C. P., & Demarque, P. 1992, *ApJS*, 78, 179
- Piskunov, N., Wood, B. E., Linsky, J. L., Dempsey, R. C., & Ayres, T. R. 1997, *ApJ*, 474, 315
- Prantzos, N. 1996, *A&A*, 310, 106
- Press, W. H., Teukolsky, S. A., Vetterling, W. T., & Flannery, B. P. 1992, *Numerical Recipes in C, the Art of Scientific Computing* (2d ed.; Cambridge: Cambridge Univ. Press)
- Rauch, M., et al. 1997, *ApJ*, 489, 7
- Rebolo, R., Beckman, J. E., & Molaro, P. 1988, *A&A*, 192, 192
- Reeves, H., Audouze, J., Fowler, W. A., & Schramm, D. N. 1973, *ApJ*, 179, 909
- Reimers, D., Koehler, S., Wisotzki, L., Grootte, D., Rodriguez-Pascual, P., & Wamsteker, W. 1997, *A&A*, 329, 270
- Rugers, M., & Hogan, C. 1996a, *ApJ*, 459, L1
- . 1996b, *AJ*, 111, 2135
- Schramm, D. N., & Turner, M. S. 1998, *Rev. Mod. Phys.*, submitted
- Scully, S., Casse, M., Olive, K. A., & Vangioni-Flam, E. 1997, *ApJ*, 476, 521
- Skillman, E. D., & Kennicutt, R. C., Jr. 1993, *ApJ*, 411, 655
- Smith, M. S., Kawano, L. H., & Malaney, R. A. 1993, *ApJS*, 85, 219
- Songaia, A., Cowie, L. L., Hogan, C. J., & Rugers, M. 1994, *Nature*, 368, 599
- Spite, F., & Spite, M. 1982, *A&A*, 115, 357
- Spite, M., Maillard, J. P., & Spite, F. 1984, *A&A*, 141, 56
- Spitzer, L., Jr. 1978, *Physical Processes in the Interstellar Medium* (New York: Wiley)
- Steigman, G. 1994, *MNRAS*, 269, 53
- Steigman, G., & Tosi, M. 1992, *ApJ*, 401, 150
- . 1995, *ApJ*, 453, 173
- Thorburn, J. A. 1994, *ApJ*, 421, 318
- Tytler, D., & Burles, S. 1997, in *Origin of Matter and Evolution of Galaxies*, ed. T. Kajino, Y. Yoshii, & S. Kubono (Singapore: World), 37
- Tytler, D., Burles, S., & Kirkman, D. 1998, *ApJ*, submitted
- Tytler, D., Fan, X.-M., & Burles, S. 1996, *Nature*, 381, 207 (TFB)
- Vangioni-Flam, E., Olive, K. A., Prantzos, N. 1994, *ApJ*, 427, 418
- Vauclair, S., & Charbonnel, C. 1995, *A&A*, 295, 715
- Wagoner, R. V., Fowler, W. A., & Hoyle, F. 1967, *ApJ*, 148, 3
- Walker, T. P., Steigman, G., Schramm, D. N., Olive, K. A., & Kang, H. S. 1991, *ApJ*, 376, 51
- Wampler, E. J., Williger, G. M., Baldwin, J. A., Carswell, R. F., Hazard, C., & McMahon, R. G. 1996, *A&A*, 316, 33
- Webb, J. K., Carswell, R. F., Lanzetta, K. M., Ferlet, R., Lemoine, M., Vidal-Madjar, A., & Bowen, D. V. 1997, *Nature*, 388, 250
- Weinberg, D. H., Miralda-Escude, J., Hernquist, L., & Katz, N. 1997, *ApJ*, 490, 564
- White, D. A., & Fabian, A. C. 1995, *MNRAS*, 273, 72
- White, S. D. M., Navarro, J. F., Evrard, A. E., & Frenk, C. S. 1993, *Nature* 366, 429
- Wolfe, A. M., Lanzetta, K. M., Foltz, C. B., & Chaffee, F. H. 1995, *ApJ*, 454, 698
- Zhang, Y., Anninos, P., Norman, M. L., & Avery, M. 1997, *ApJ*, 485, 496